Schaffer, B., Grogger, W., Kothleitner, G. and Hofer, F. (2010) *Comparison of EFTEM and STEM EELS plasmon imaging of gold nanoparticles in a monochromated TEM*. Ultramicroscopy, 110 (8). pp. 1087-1093. ISSN 0304-3991

http://eprints.gla.ac.uk/38354

Deposited on: 21 October 2010

Enlighten – Research publications by members of the University of Glasgow
http://eprints.gla.ac.uk

Comparison of EFTEM and STEM EELS plasmon imaging of gold nanoparticles in a monochromated TEM

Bernhard Schaffer[1,2,3*], Werner Grogger[1], Gerald Kothleitner[1], Ferdiand Hofer[1]

[1] Institute for Electron Microscopy and Fine Structure Research, Graz University of Technology, 8010 Graz, Austria

[2] SuperSTEM Laboratory, STFC Daresbury, WA4 4AD Warrington, United Kingdom

[3] Department of Physics and Astronomy, University of Glasgow, G12 8QQ Glasgow, United Kingdom

[*] corresponding author; Tel.: +44 1925 864 902 ; fax: +44 1925 864 910

eMail: b.schaffer@physics.gla.ac.uk

Abstract

We present and compare two different imaging techniques for plasmonic excitations in metallic nanoparticles based on high energy-resolution electron energy-loss spectroscopy in a monochromated transmission electron microscope. We demonstrate that a recently developed monochromated energy-filtering (EFTEM) approach can be used in addition to the well established scanning technique to directly obtain plasmon images in the energy range below 1 eV. The EFTEM technique is described in detail, and a double experiment performed on the same, triangular gold nanoparticle compares equivalent data acquired by both techniques, respectively.

Keywords

EFTEM, EELS, spectrum-imaging, plasmon, nano-particle, monochromator

Introduction

Optical properties of gold nanoparticles (Au-NPs) have been utilized for millennia [1], but it was not until the work of Gustav Mie [2] that a proper theoretical background for this behavior was described [3,4]. The current interest in metallic nanoparticles (Me-NPs) stems strongly from their manifold application as 'tunable' sensors [5,6,7]. It is well known, that particle size and shape [8] as well as the local dielectric environment [9] and nearby Me-NPs [10,11,12] have strong impact on the optic properties of Me-NPs, and are thus parameters for custom-tailoring their behavior.

Spatially resolved measurements of the optical response of Me-NPs have been carried out with optical near-field microscopes [13,14,15,16], but a higher spatial resolution can be gained by transmission electron microscopy (TEM) via electron energy-loss spectroscopy (EELS). The dielectric function ε of the material can be derived from the energy-loss of the transmitted electrons, and – in the absence of intra-band transitions of single electrons – optical absorption can be understood as excitation process of collective oscillations of the conduction electrons (plasmons) which are directly observable in an EELS spectrum. In particular surface plasmons, oscillations propagating along the specimen surface, have their resonance frequencies in the visible spectrum, which corresponds to energy-loss values of 1.65 to 3.25 eV.

In the last fifteen years EELS spectrum-imaging techniques [17] have been well developed and are now available on a nearly routine basis in most analytical TEMs. Spectrum-imaging (SI) acquires complete spectral information for all spatially resolved positions in a field-of-

view (FOV). Consequently, spectral features such as surface plasmon peaks can be analyzed as function of position, and according images and maps can be produced. While there are two different routes in which EELS SI data can be acquired, the more commonly applied technique uses scanning TEM (STEM) to sequentially acquire spectra from each spatial position probed by a focused beam. The technique is accordingly called STEM EELS SI. In the alternative technique, the sample is illuminated by a parallel beam and energy-filtering TEM (EFTEM) imaging is used to acquire image series of adjacent energy intervals [18]. This technique is referred to as EFTEM SI. In this work we present and compare data acquired from identical Au-NPs by both techniques.

In general, STEM EELS SI offers the more direct approach from a spectroscopic viewpoint. It currently offers the best energy-resolution, is easily set up, and is available in all systems with scanning capabilities and any kind of EELS detector. In modern microscopes, the spatial resolution is no longer limited by the smallest achievable electron probe size alone, but can also be restricted by physical limitations of the experiment itself [19]. Successful surface plasmon maps by STEM EELS SI have been reported for triangular shaped Ag-NPs with a side length of ~80 nm [20], and for spherical or ellipsoidal Ag-NPs and elongated Au-NPs [21,22,23,24]. This type of experiment is especially challenging if surface plasmon peaks are to be observed at low energy-loss values <2 eV where the tails of the intense zero-loss peak (ZLP) already hamper easy detection. The problem can be overcome by improving the energy resolution (and thus the width of the ZLP) of the system. In a monochromated system with an energy resolution of 250 meV or better, Au-NP surface plasmon peaks at 0.8 eV can be easily detected without data deconvolution techniques [25].

EFTEM SI is most often used as an EELS imaging technique for moderate to low energy-resolution (1-50 eV). However, using a sufficiently small energy selecting slit width enables data acquisition with energy resolution below 1 eV down to the intrinsic energy-resolution of the system [26], and systems equipped with a monochromator have recently been used for EFTEM imaging of plasmon peaks close to the ZLP with an energy resolution of 0.5 eV or better [27,28,29]. Switching between STEM EELS and EFTEM mode can be achieved with relative ease, allowing the direct comparison of data from the same particle. Publications so far have compared data locally [27,28]. In this work the comparison of whole maps is shown.

Experimental

Sample preparation

The Au-NPs were synthesized by a modification of the conventional citrate reduction of gold salt in water [30,31], using purified water and chemicals as received from the given suppliers. Hydrogentetrachloroaurate(III)trihydrate ($HAuCl_4$ $3H_2O$ > 99.5%) was obtained from Carl Roth GmbH, while Trisodium citrate dihydrate (99%) and sodium chloride (NaCl; 99.5%) were purchased from Merck. The final particle solution consisted of 1 ml $HAuCl_4$-solution (2.5 mM), 25 µl sodium citrate (0.1 M), 0.5 ml sodium chloride (5 M) and 8.5 ml water. It was dropped on a carbon-coated copper grid, and the liquid was allowed to evaporate at room temperature. The final TEM sample consists of differently shaped and sized NPs, but this investigation concentrated on nano-triangles. In particular, one truncated equilateral triangle with a side-length of 280 nm and a thickness of about 20 nm was studied in this work (Figure 1).

Monochromated STEM EELS SI

The STEM EELS SI measurement was carried out using the Tecnai F20 (FEI Company) system installed at the Graz University of Technology, Austria. This system has a super twin objective lens (C_c=1.2 mm C_s=1.2 mm) and is optimized for high energy resolution using a Wien-filter monochromator, an improved high tension tank, active triaxial magnetic field compensation, and the High Resolution Gatan Imaging Filter with an UltraScan 2k CCD camera. Digiscan II (Gatan Inc.) and a high angle annular dark field (HAADF) detector (Fischione) are used during STEM operation of the microscope. All STEM EELS SI measurements were carried out in monochromated mode, using a camera length of 300 mm, a convergence half angle α of 11.4 mrad, and a collection half angle β of 2.0 mrad. The spectrometer dispersion was set to 0.005 eV/channel, and an exposure time of 0.2 sec per spectrum was used for the acquisition of the 64x64 pixel STEM EELS SI. Online spatial drift correction was performed after each line of the SI, and the total acquisition time was 54 min. Figure 1a and 1b show the STEM bright field (BF) and HAADF image of the analyzed Au-NP triangle, respectively. Areas used for SI data acquisition and spatial drift correction are indicated. The spatial resolution of the SI data is limited by the sampling distance of 5.4 nm which is roughly twice the electron probe diameter of 2.8 nm. The energy resolution measured as the full-width at half-maximum (FWHM) value of the ZLP in vacuum was 0.22 eV. After data acquisition, the individual spectra were aligned to each other using the maximum of the ZLP as a reference. No other data treatment was applied.

Monochromated EFTEM SI

EFTEM SI was performed using the same system as described above immediately after the STEM EELS SI measurements. Figure 1c shows a zero-loss filtered TEM bright field image of the particle after the STEM EELS SI but before the EFTEM SI measurement. In comparison to the well established EFTEM SI routines for medium energy resolution, monochromated EFTEM SI has to consider some additional aspects:

First, the illumination has to be set to a parallel, but monochromated beam. In the used system, this is achieved by adjustment of the condenser lens after aligning the monochromator and its slit by the conventional routines using a dispersed 'rainbow' illumination. Lacking an additional degree of freedom as would be provided by an additional lens, our current system does not allow an independent choice of the size of the illuminated area while working in monochromated, parallel illumination. FOVs are thus limited to <400 nm, and current density can not be optimized for highest magnifications.

Second, the energy range selected by the slit of the imaging filter (GIF slit width) has to be accurately calibrated. In the post-column filter this is done by observing an EELS spectrum in spectroscopy mode, using a well calibrated dispersion setting which produces a focused spectrum in the plane of the energy-selecting slit. Thus, the exact slit width can then be measured by inserting the slit and observing the points of inflection in the EEL spectrum. Figure 2 compares EEL spectra of the holey carbon film acquired at 0.01eV/px dispersion in the low-loss regime where no spectral features appear and the background is sufficiently linear. For monochromated EFTEM SI experiments, the calibrated slit was set to 0.3 eV.

Third, exposure times have to be adjusted during acquisition. For EFTEM SI data acquired across or close to the ZLP the variation in intensity is much larger than the dynamic range of the CCD detector at any single exposure time. This is particularly true for monochromated electron sources with a narrow Gauss-distribution of the primary energy. Exposure times preventing saturation or overexposure at the ZLP are too short for a sufficient signal-to-noise ratio (SNR) in the adjacent low energy-loss region. However, EFTEM SI as a serial acquisition technique in the energy-domain allows adjustment of exposure times as a function of energy-loss, effectively increasing the dynamic range of the detector [32]. Theoretically, an optimum exposure could be calculated from a ZLP model (or experimental spectrum) as a function of energy position and slit width, but this is not practical for two reasons: First, because system instabilities may cause deviations from the nominal energy position (i.e. energy drift), and second, because lens aberrations in the imaging filter cause the iso-energy planes to be curved, so that different parts of the CCD detect electrons of slightly different energy (i.e. non-isochromaticity). Therefore, we have developed our own EFTEM SI

acquisition package written in the Digital Micrograph script language which automatically adapts exposure times to the encountered intensity situation without a priori information.
Forth, monochromated EFTEM SI yields an energy resolution at which aberrations of the imaging filter and system instabilities are no longer negligible, and additional data correction becomes necessary [33]. These corrections are implemented in our EFTEM SI package.

EFTEM SI data acquisition and correction routine

This section generally describes our software package used for acquisition and correction of EFTEM SI data. Details for the specific Au-NP triangle dataset are given at the end. The main goal of the 'Automated EFTEM Acquisition' (AEA) routine is to quickly adjust the exposure times of each image to an optimum. The user is asked to provide the following main parameters: The standard parameters slit width, energy range and energy step size; a goal intensity range defined by a lower and an upper limit; a range of allowed exposure times for a single image acquisition; a range for the number of frame-readouts at a particular energy-loss; and a trigger time, which is used to influence the algorithm to either prefer multiple frames or longer exposure times to increase intensity at an energy step. Exposures above the trigger time are preferably optimised by multiple frames. The idea is to allow automated adjustments for both high- and low-intensity situations. For a high-intensity situation, when exposure times are generally low, adjustment is primarily done by increasing exposure times. However, for a low-intensity situation, multiple frames are preferred and can be corrected for sample drift prior to summing which reduces drift-induced blurring. Independent of whether multiple frames or increased exposure time is preferred, the alternative method will be used by the algorithm if necessary.
At the start, the AEA algorithm acquires all necessary dark references in advance by default. This allows fast changes of exposure times during the acquisition of the data. However, if dark reference noise is a limiting factor or constant dark current can not be assumed (e.g. due to after-glowing effects), individual dark references can optionally be acquired for each exposure at the cost of strongly increased total acquisition time. After dark reference acquisition, the starting energy-loss and slit width is set, and a few seconds are waited, before the EFTEM SI is acquired step by step. For each energy step, an image with a testing acquisition time is first recorded without dark current/gain correction, and the saturated or overexposed pixels are counted. If this number exceeds an allowed number of 'hot' pixels, the image is rejected as overexposed, exposure time is reduced, and the CCD is read out quickly several times to reduce after-glow effects. This step of the algorithm is a safety measure to

prevent detector damage, but saturation and overexposure is generally avoided by the algorithm aiming for moderate intensity levels. If the test image is not considered overexposed, the routine will next perform a dark current subtraction and gain normalisation. It checks for underexposure by counting pixels below the level of dark current noise, and will start again with a test image of higher exposure time if needed and possible. If the test image is neither over- nor underexposed, the routine will calculate the intensity level of the image by taking the mean value of the 'brightest' pixels excluding statistical outliers. If needed, exposure time will be adjusted to achieve a value within the wanted intensity range for the sum image of used frame readouts. Any change of exposure time triggers checks for over- and underexposure anew. Once the optimum exposure time is found, all frames of the current energy step are acquired. Images are saved to the hard disc at once to keep the system memory free, and to allow stopping the acquisition without loosing already acquired data. Acquisition parameters needed for later data processing are stored as image tags, and the procedure continues with the next energy step. If the achieved mean intensity in the last frame is above the maximum goal intensity, the next energy step will be tried with a shorter exposure time to speed up acquisition. Otherwise, the current exposure time will be kept.

While the AEA routine is a fully automated routine, user interaction is possible during acquisition. The last acquired image, a plot of total intensity sum, and a log of performed actions is always displayed for information, and a little dialog window gives the opportunity to interactively adjust the required intensity levels, to force a number of readouts per energy step regardless of the intensity situation, or to pause the acquisition in order to manually correct for spatial drift.

After AEA acquisition, all stored images are processed into a fully corrected EFTEM SI dataset by additional routines. Missing images – because of an interrupted acquisition or because individual images have been manually removed as 'invalid' – do not prevent correct processing of the existing data. For a full correction, information on non-isochromaticity, spatial drift, and energy drift needs to be gathered. The first can either be gained as a result of the GIF tuning routine, or by mapping the energy position of a known feature (e.g. the ZLP) from the raw data. Optionally, the aberration function can be smoothed or interpolated by a polynomial fit of higher order. Spatial drift is usually determined by cross-correlating the acquired images, and we use the SDSD software [34]. Energy drift is determined by assuming time-linear behaviour and measuring before and after the experiment. The correction algorithm automatically interpolates this time-linear energy drift for each of the acquired images. In a final step, all available information (i.e. varying exposure time, varying number

of readouts, spatial drift, energy drift, non-isochromaticity) is used to map the acquired data into a corrected, three-dimensional EFTEM SI data cube using weighted sums. The processing time for a typical data set of about 200 MB is less than one minute on a modern desktop PC. It should be noted that the quality of the correction depends strongly on the sampling of the data, which is generally good for the spatial domain but less so for the energy axis.

The EFTEM SI of the triangular Au-NP was acquired and corrected by the described routines. 60 energy steps of 0.1 eV covering the range from 4.5 eV down to -1.5 eV were used and 97 individual images with exposure times between 0.08 and 10.24 sec were recorded over a total acquisition time of 11 min. Only the central 1024x1024 pixel area of the CCD was used, and 2x2 binning was enabled, giving a final image size of 512x512 pixels and a pixel size of 0.89 nm. Figure 3 shows the parameters used for data correction. The non-isochromaticity was 0.16 eV peak-to-peak, total spatial drift was less than 4 nm, and total energy drift which has then been time-linearly interpolated was 1.1 eV.

results

Figure 4 compares the energy resolution of the two techniques. The ZLP was extracted over the whole FOV from both final datasets. Due to the coarse sampling, a Gaussian has been fit to the EFTEM SI data before deriving the FWHM value. The according energy resolutions are 0.22 eV and 0.40 eV for STEM and EFTEM, respectively. In case of STEM EELS, the energy resolution has been measured to the same value on a single spectrum acquired in vacuum with 0.2 sec exposure time. The STEM EELS SI and the EFTEM SI results of an identical Au-NP triangle are shown in Figures 5 to 10. Each of the figures compares the equivalent extracted plasmon images from both datasets at the given energy-loss value. Those images represent the integrated EELS intensity of the raw dataset over an energy interval of 0.3 eV. In case of the EFTEM SI, the intensity has been extracted from a single energy-channel at the given energy-loss as indicated in the corresponding spectrum. In case of the STEM EELS SI, 60 channels representing 0.3 eV have been integrated at the same central energy-loss value. Contrast has been inverted in the images for better visibility such that dark areas represent areas of higher intensity. Next to the maps, each figure compares the extracted spectra from both datasets. The according extraction positions are indicated as white squares in the maps. 4x4 and 24x24 pixels have been integrated in case of STEM EELS SI and EFTEM SI, respectively.

The data of both datasets matches generally very well, demonstrating that both techniques can be used to access the same specimen information. However, it should be noted that although the data was acquired from the same Au-NP, some circumstances (i.e. the orientation of the

particle with respect to the electron beam; contamination and/or beam damage; a slight bending of the flat particle) have slightly changed and may have caused subtle differences in the data. This is also apparent in the comparison of the bright field images in figure 1a and 1c. In both datasets the same complex behaviour with respect to plasmon peak maxima can be observed. The threefold symmetry of the particle is only partially preserved in the imaged plasmonic modes, probably due to the fact, that the particle is only partially supported by the carbon. The TEM bright-field image (Figure 1c) also shows some inhomogeneity in the bottom right corner of the triangle, and its EELS spectrum (Figure 6) differs strongly from the top right corner (Figure 5). Figure 11 shows 26 spectra along the upper edge of the triangle extracted from STEM EELS SI data. It shows the asymmetric shift of the maximum position of the broad peak between 1.5 and 2.2 eV which can also be observed in the plasmon images.

Conclusion

We have shown that both STEM EELS SI and EFTEM SI can be applied on direct plasmon imaging of Au-NPs in the very low energy-loss region provided a sufficient energy resolution can be achieved. A monochromated system, which not only reduces the FWHM of the ZLP, but also substantially decreases intensity in the tails of the ZLP, is well suited for direct imaging of plasmon peaks below 1 eV energy-loss without the need of data deconvolution.

We described in detail the technique of monochromated EFTEM SI, which has recently been developed, and compared two datasets acquired from the same triangular Au-NP by both EFTEM SI and STEM EELS SI. By comparison of spectra and maps we could directly demonstrate the equality of both methods in terms of principal results while at the same time highlighting their advantages and disadvantages.

While the STEM approach yields higher energy resolution and thus allows accurate mapping of peak positions, the EFTEM approach provides spatially highly resolved information over large FOVs in comparably short acquisition time. It is therefore the ideal technique to study long distance effects as encountered in coupled systems.

Our work primarily concentrated on the methodical aspect of plasmon mapping of metallic nanoparticles in the very low energy-loss regime, as it has been recently become available. A thorough physical interpretation of the measured effects was not aimed for and requires further optimized experiments with well controlled sample parameters.

figure captions

Figure 1: STEM BF (a), STEM HAADF (b), and zero-loss filtered TEM BF (c) of a triangular Au-NP. The region of STEM EELS SI acquisition and spatial drift correction is indicated. The TEM BF image (c) was acquired in between STEM EELS SI and EFTEM SI acquisition.

Figure 2: EEL spectrum of a holey carbon film at 0.01 eV/pixel dispersion with inserted energy selecting slit and different slit widths used for calibration (see text). The zero of the energy-loss axis is set to the left points of inflection which correspond to xxx eV "real" energy loss.

Figure 3: Parameters used for final EFTEM SI data correction of the Au-NP data. The system's non-isochromaticity (left) was determined by the filter tuning routine, spatial and energy-drift (right) were determined from the raw data set

Figure 4: Zero-loss peaks extracted from the whole FOV for both EFTEM SI and STEM EELS SI data. Intensity has been normalized for better comparison of energy resolution.

Figure 5: Plasmon images with inverted intensity scale extracted at 1.0 eV energy-loss: from STEM EELS SI (a) and from EFTEM SI (b) . Extracted energy-loss spectra (c) from both datasets at the indicated position.

Figure 6: Plasmon images with inverted intensity scale extracted at 1.0 eV energy-loss: from STEM EELS SI (a) and from EFTEM SI (b) . Extracted energy-loss spectra (c) from both datasets at the indicated position.

Figure 7: Plasmon images with inverted intensity scale extracted at 1.6 eV energy-loss: from STEM EELS SI (a) and from EFTEM SI (b) . Extracted energy-loss spectra (c) from both datasets at the indicated position.

Figure 8: Plasmon images with inverted intensity scale extracted at 1.6 eV energy-loss: from STEM EELS SI (a) and from EFTEM SI (b) . Extracted energy-loss spectra (c) from both datasets at the indicated position.

Figure 9: Plasmon images with inverted intensity scale extracted at 1.8 eV energy-loss: from STEM EELS SI (a) and from EFTEM SI (b) . Extracted energy-loss spectra (c) from both datasets at the indicated position.

Figure 10: Plasmon images with inverted intensity scale extracted at 2.0 eV energy-loss: from STEM EELS SI (a) and from EFTEM SI (b) . Extracted energy-loss spectra (c) from both datasets at the indicated position.

Figure 11: Extracted energy-loss spectra from the STEM EELS SI along the edge of the triangle as indicated by the white arrow. Spectra have been smoothed by a running average filter for better visibility. The map shows the integrated intensity from 0.5 to 3.0 eV.

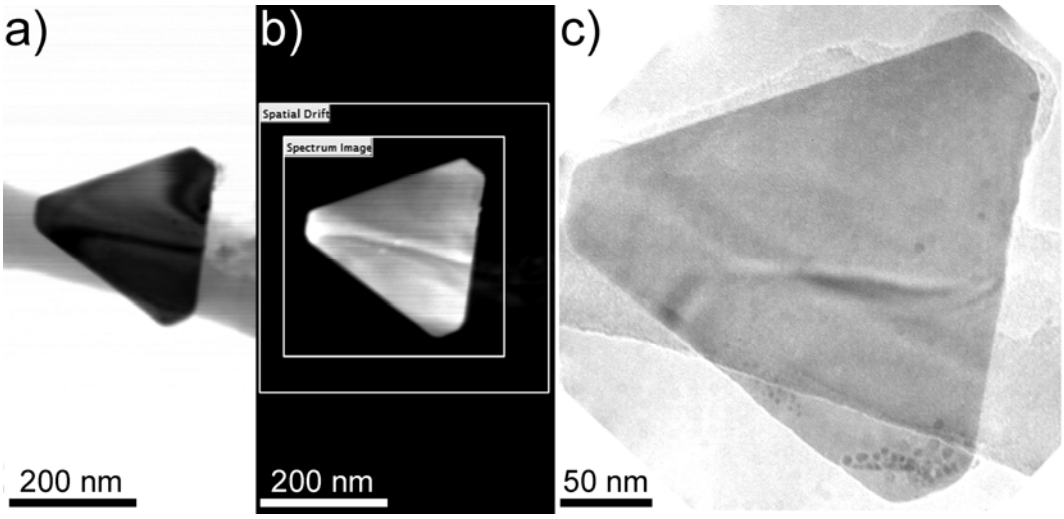

Figure 1: STEM BF (a), STEM HAADF (b), and zero-loss filtered TEM BF (c) of a triangular Au-NP. The region of STEM EELS SI acquisition and spatial drift correction is indicated. The TEM BF image (c) was acquired in between STEM EELS SI and EFTEM SI acquisition.

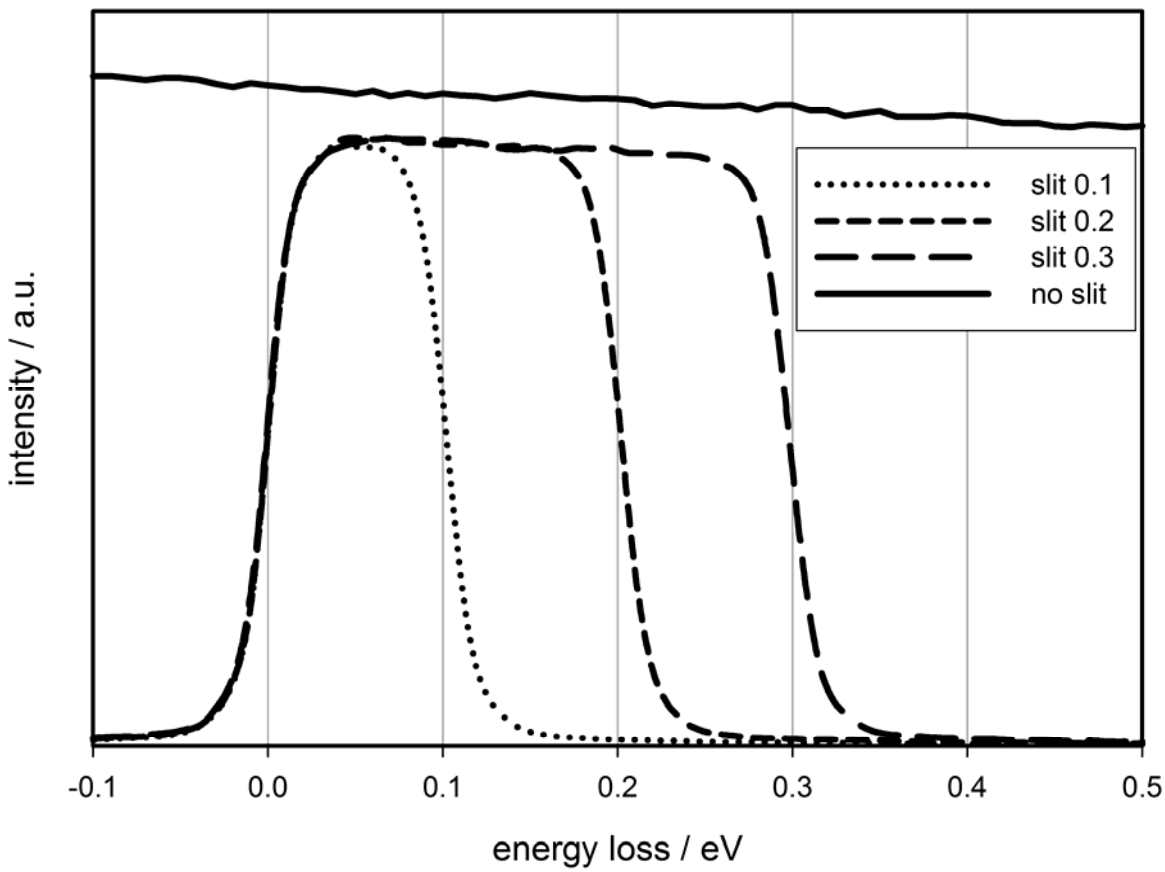

Figure 2: EEL spectrum of a holey carbon film at 0.01 eV/pixel dispersion with inserted energy selecting slit and different slit widths used for calibration (see text). The zero of the energy-loss axis is set to the left points of inflection which correspond to xxx eV “real” energy loss.

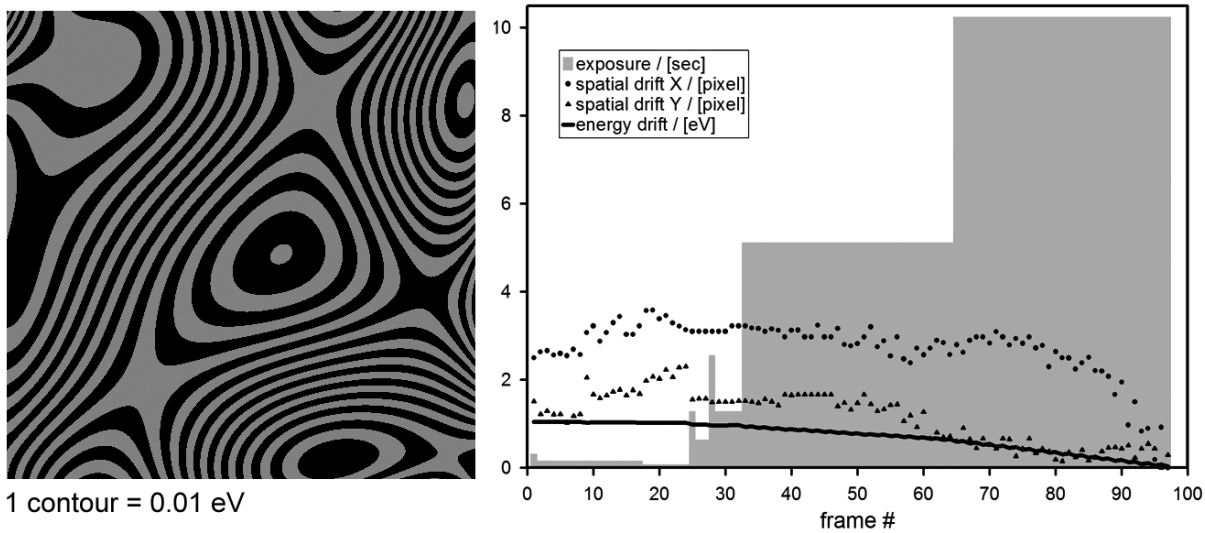

Figure 3: Parameters used for final EFTEM SI data correction of the Au-NP data. The system's non-isochromaticity (left) was determined by the filter tuning routine, spatial and energy-drift (right) were determined from the raw data set

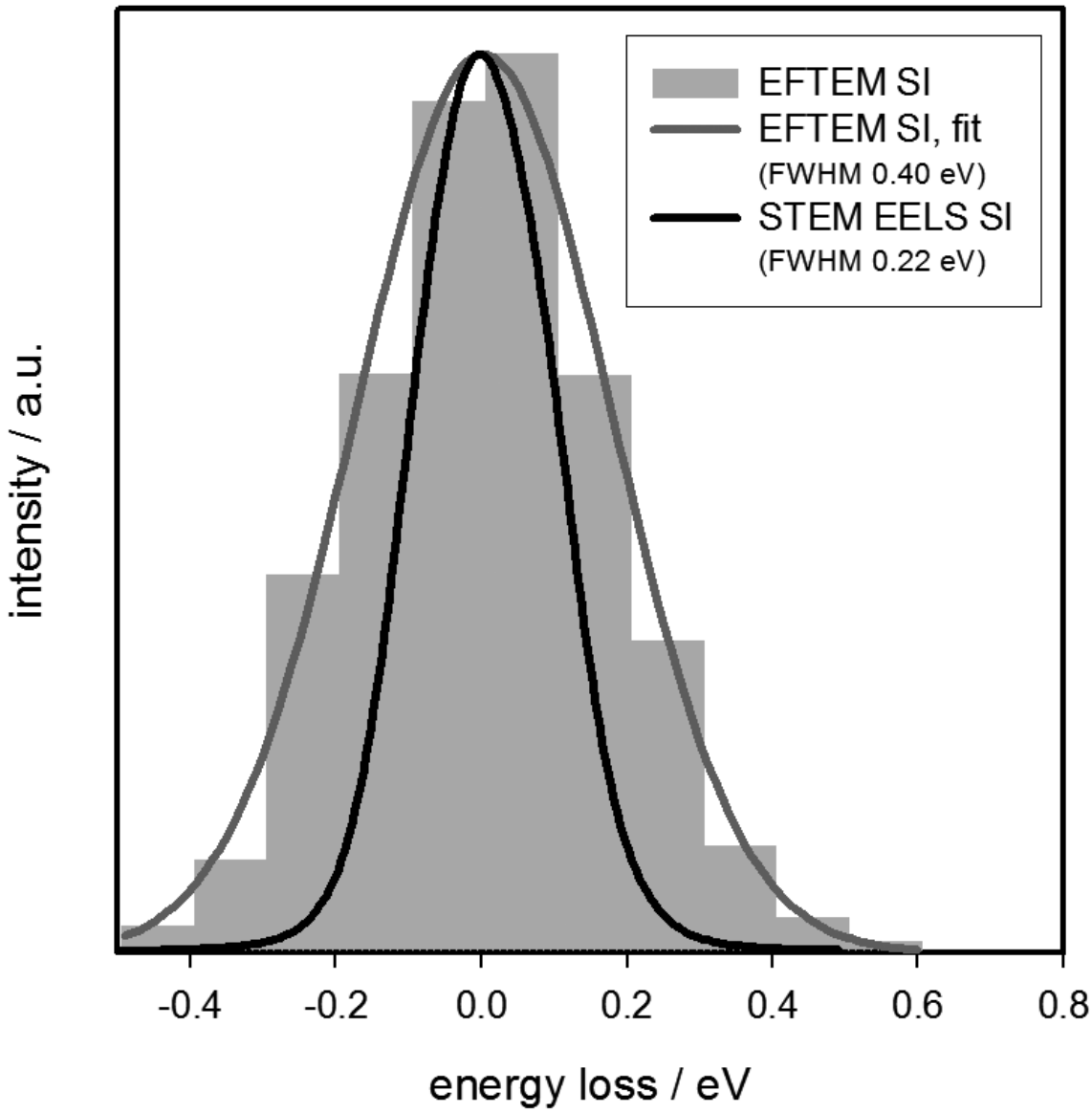

Figure 4: Zero-loss peaks extracted from the whole FOV for both EFTEM SI and STEM EELS SI data. Intensity has been normalized for better comparison of energy resolution.

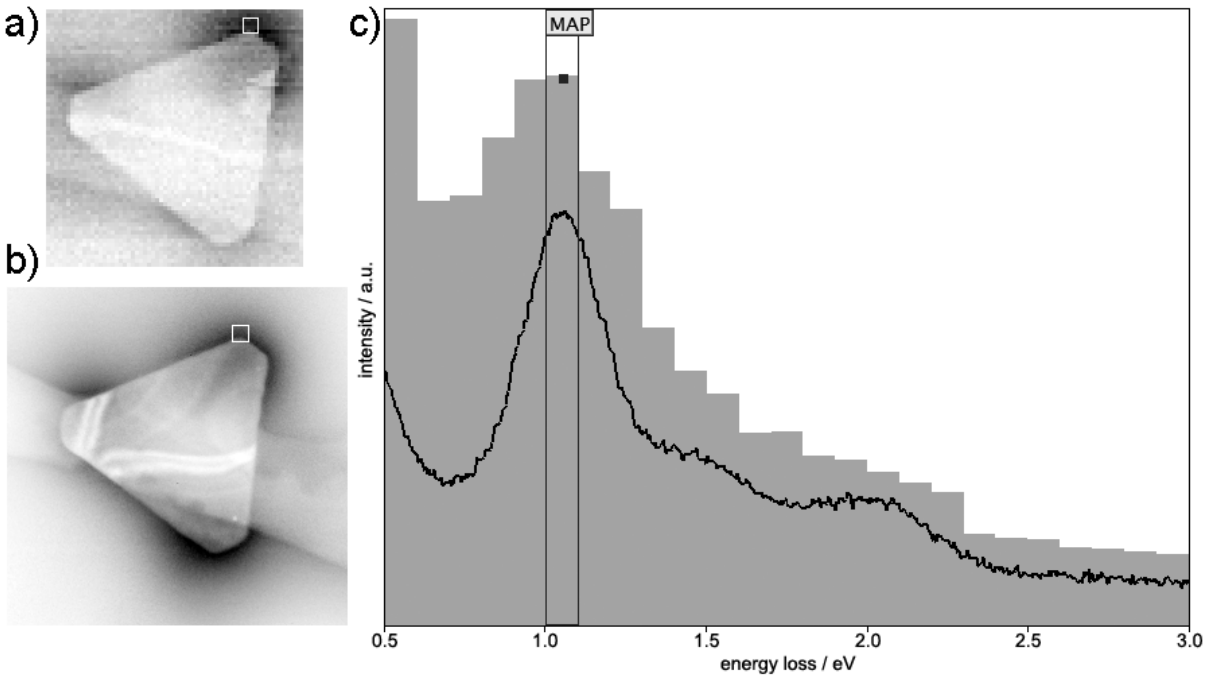

Figure 5: Plasmon images with inverted intensity scale extracted at 1.0 eV energy-loss: from STEM EELS SI (a) and from EFTEM SI (b) . Extracted energy-loss spectra (c) from both datasets at the indicated position.

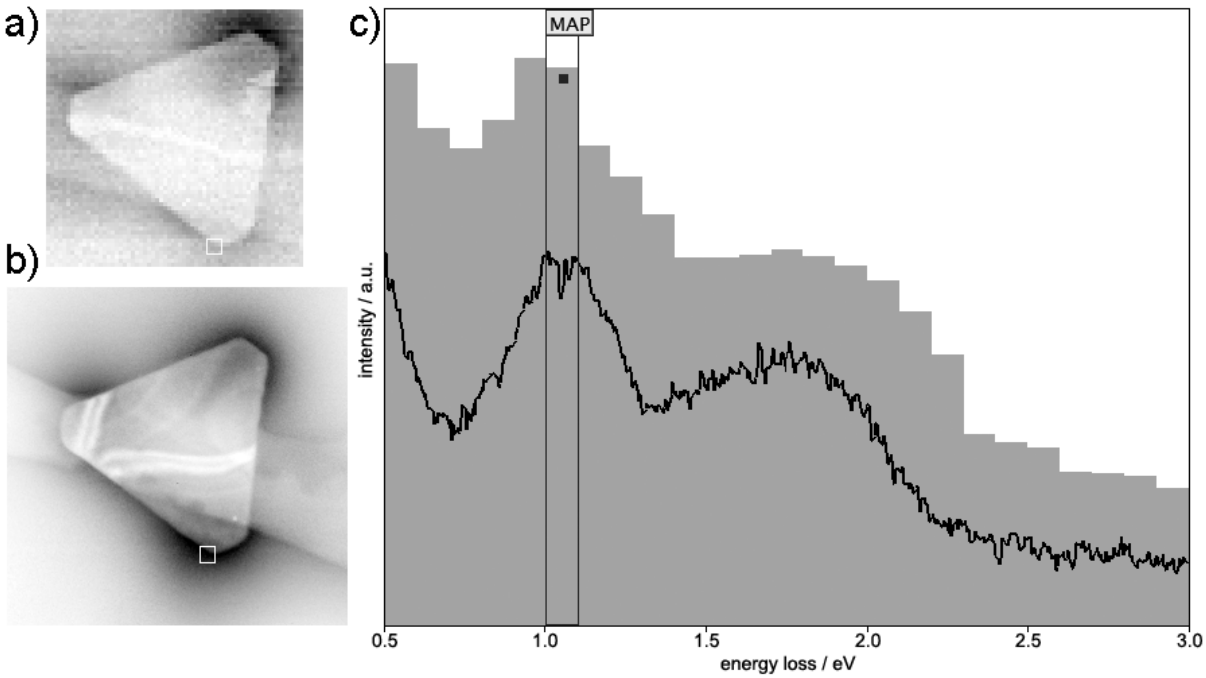

Figure 6: Plasmon images with inverted intensity scale extracted at 1.0 eV energy-loss: from STEM EELS SI (a) and from EFTEM SI (b) . Extracted energy-loss spectra (c) from both datasets at the indicated position.

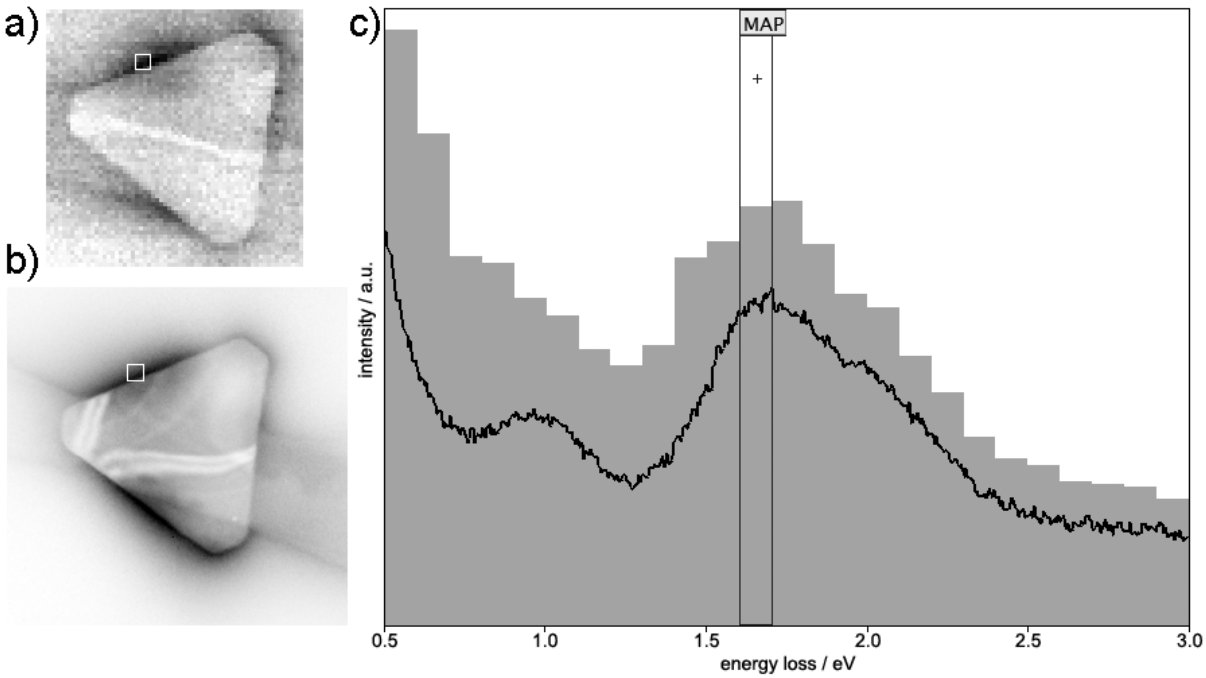

Figure 7: Plasmon images with inverted intensity scale extracted at 1.6 eV energy-loss: from STEM EELS SI (a) and from EFTEM SI (b) . Extracted energy-loss spectra (c) from both datasets at the indicated position.

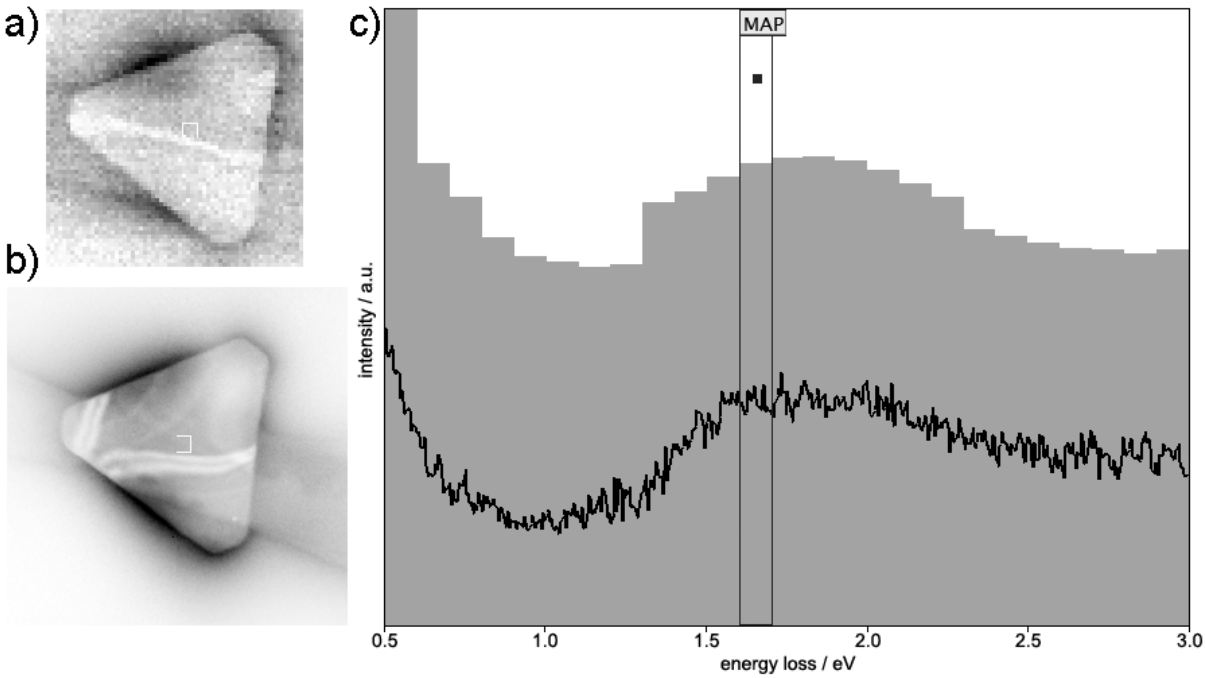

Figure 8: Plasmon images with inverted intensity scale extracted at 1.6 eV energy-loss: from STEM EELS SI (a) and from EFTEM SI (b) . Extracted energy-loss spectra (c) from both datasets at the indicated position.

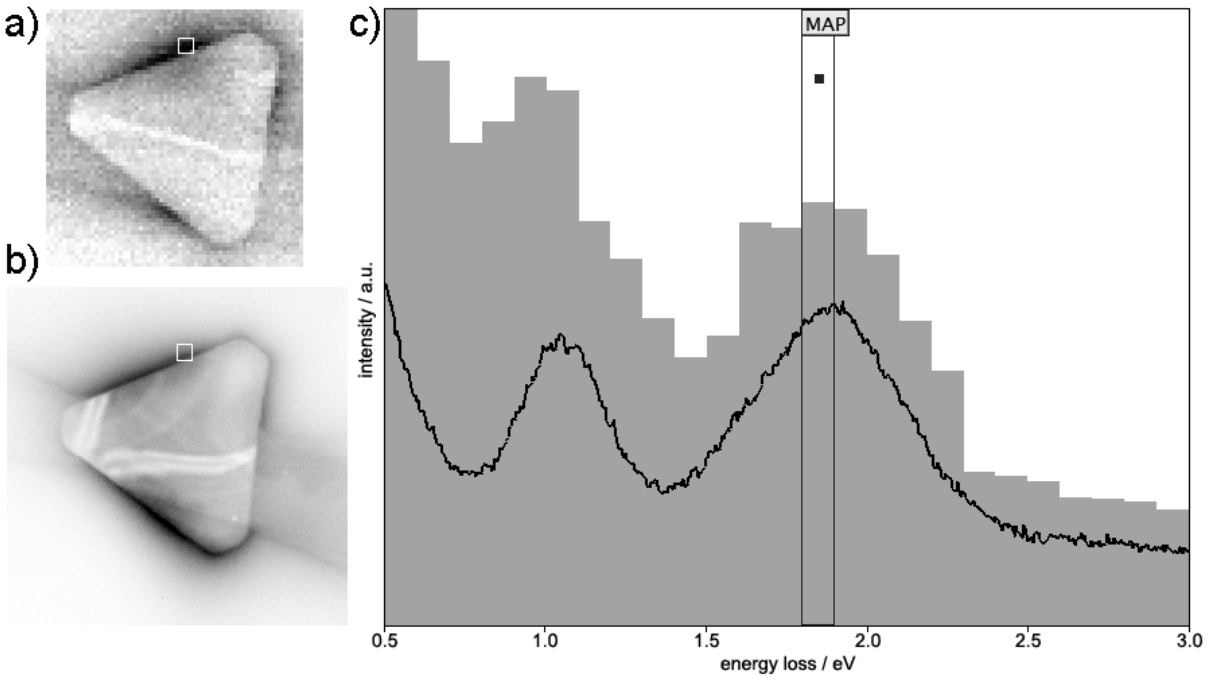

Figure 9: Plasmon images with inverted intensity scale extracted at 1.8 eV energy-loss: from STEM EELS SI (a) and from EFTEM SI (b) . Extracted energy-loss spectra (c) from both datasets at the indicated position.

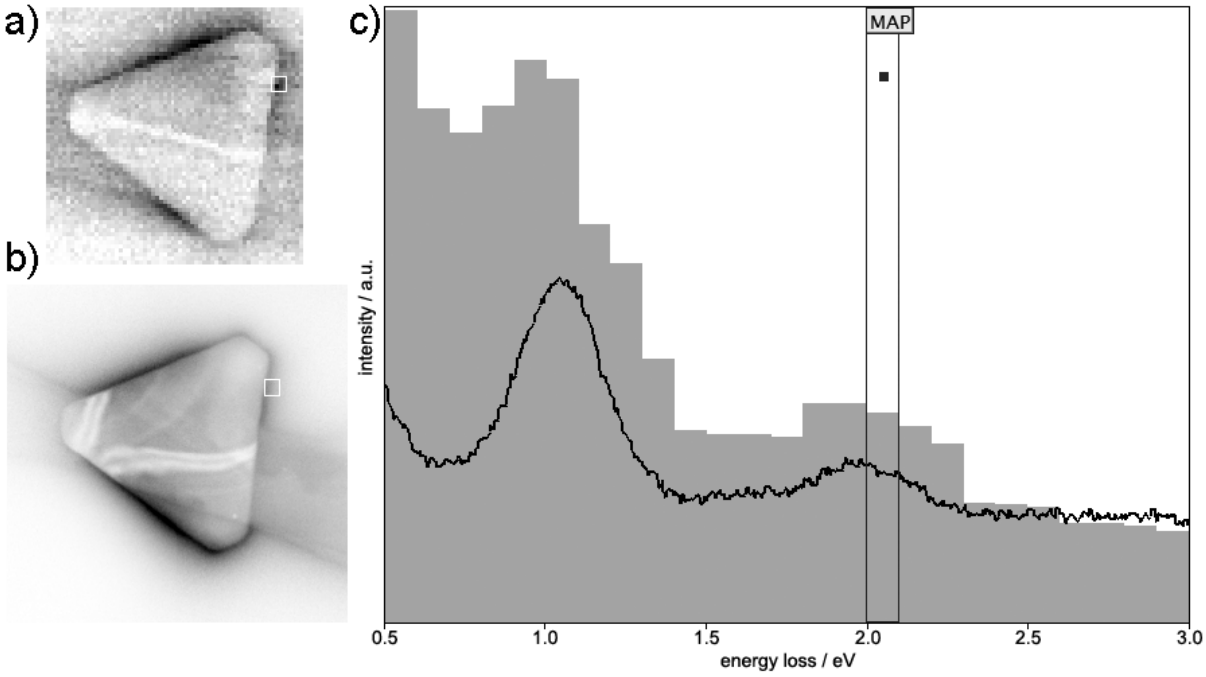

Figure 10: Plasmon images with inverted intensity scale extracted at 2.0 eV energy-loss: from STEM EELS SI (a) and from EFTEM SI (b) . Extracted energy-loss spectra (c) from both datasets at the indicated position.

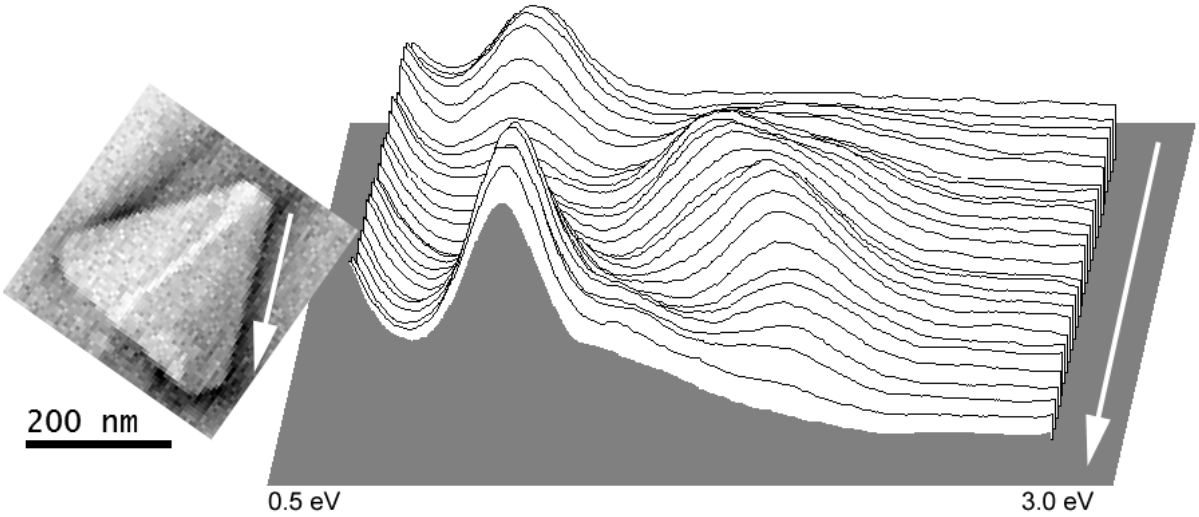

Figure 11: Extracted energy-loss spectra from the STEM EELS SI along the edge of the triangle as indicated by the white arrow. Spectra have been smoothed by a running average filter for better visibility. The map shows the integrated intensity from 0.5 to 3.0 eV.

References

[1] I. Freestone, N. Meeks, M. Sax, C. Higgitt, Gold Bulletin 40 (2007) 270.

[2] G. Mie, Annalen der Physik 330 (1908) 377.

[3] M. Kerker, The scattering of light, and other electromagnetic radiation, Academic Press, New York, 1969.

[4] M. Kerker, Journal of Colloid and Interface Science 105 (1985) 297.

[5] A. Haes, D. Stuart, S. Nie, R. Van Duyne, Journal of Fluorescence 14 (2004) 355.

[6] N. Nath and A. Chilkoti, Journal of Fluorescence 14 (2004) 377.

[7] T. Kalkbrenner, M. Ramstein, J. Mlynek, V. Sandoghdar, J. Microsc. 202 (2001) 72.

[8] P.G. Evans, A. Passian, T. L. Ferrell, Ultramicroscopy 107 (2007) 1012.

[9] T.R. Jensen, M. L. Duval, K. L. Kelly, A. A. Lazarides, G. C. Schatz, R. P. Van Duyne, J. Phys. Chem. B 103 (1999) 9846.

[10] J. Aizpurua, G. W. Bryant, L. J. Richter, F. J. G. de Abajo, B. K. Kelley, T. Mallouk, Phys. Rev. B. 71 (2005) 235420.

[11] T. Atay, J. H. Song, A. V. Nurmikko, Nano Lett. 4 (2004) 1627.

[12] G.W. Bryant, I. Romero, F. J. G. de Abajo, J. Aizpurua, 6323 (2006) 632313.

[13] T. Klar, M. Perner, S. Grosse, G. von Plessen, W. Spirkl, J. Feldmann, Phys. Rev. Lett. 80 (1998) 4249.

[14] S. Ducourtieux, V. A. Podolskiy, S. Gr sillon, S. Buil, B. Berini, P. Gadenne, A. C. Boccara, J. C. Rivoal, W. D. Bragg, K. Banerjee, V. P. Safonov, V. P. Drachev, Z. C. Ying, A. K. Sarychev, V. M. Shalaev, Phys. Rev. B 64 (2001) 165403.

[15] R. Hillenbrand and F. Keilmann, Applied Physics B: Lasers and Optics 73 (2001) 239.

[16] A. Hohenau, J. R. Krenn, H. Ditlbacher, A. Leitner, F. R. Aussenegg, W. L. Schaich, Europhysics Letters 69 (2005) 538.

[17] C. Jeanguillaume and C. Colliex, Ultramicroscopy 28 (1989) 252.

[18] J.-L. Lavergne, J.-M. Martin, M. Belin, Microsc. Microanal. Microstruct. 3 (1992) 517.

[19] R.F. Egerton, J. Electron. Microsc. 48 (1999) 711.

[20] J. Nelayah, M. Kociak, O. Stephan, F. J. Garcia de Abajo, M. Tence, L. Henrard, D. Taverna, I. Pastoriza-Santos, L. M. Liz-Marzán, C. Colliex, Nature Physics 3 (2007) 348.

[21] M. Bosman, V. J. Keast, M. Watanabe, A. I. Maaroof, M. B. Cortie, Nanotechnology 18 (2007) 165505.

[22] M. Gom, J. Ringnalda, J. F. Mansfield, A. Agarwal, N. Kotov, N. J. Zaluzec, T. B. Norris, Nano Lett. 8 (2008) 3200.

[23] M.W. Chu, V. Myroshnychenko, C. H. Chen, J. P. Deng, C. Y. Mou, F. J. Garcia de Abajo, Nano Lett. 9 (2008) 399.

[24] A.L. Koh, K. Bao, I. Khan, W. E. Smith, G. Kothleitner, P. Nordlander, S. A. Maier, D. W. McComb, ACS Nano 3 (2009) 3015.

[25] B. Schaffer, K. Riegler, G. Kothleitner, W. Grogger, F. Hofer, Micron 40 (2009) 269.

[26] B. Schaffer, W. Grogger, G. Kothleitner, F. Hofer, Analytical and Bioanalytical Chemistry 390 (2008) 1439.

[27] B. Schaffer, U. Hohenester, A. Trugler, F. Hofer, Physical Review B (Condensed Matter and Materials Physics) 79 (2009) 041401.

[28] J. Nelayah, L. Gu, W. Sigle, C. T. Koch, I. Pastoriza-Santos, L. M. Liz-Marzán, P. A. van Aken, Opt. Lett. 34 (2009) 1003.

[29] W. Sigle, J. Nelayah, C. T. Koch, P. A. van Aken, Opt. Lett. 34 (2009) 2150.

[30] J. Turkevich, P. C. Stevenson, J. Hillier, Discussion of the Faraday Society 11 (1951) 55.

[31] K. Riegler, Thesis/Dissertation (2005) Synthesis and characterization of gold nanoparticles.

[32] P.J. Thomas and P. A. Midgley, Ultramicroscopy 88 (2001) 187.

[33] B. Schaffer, G. Kothleitner, W. Grogger, Ultramicroscopy 106 (2006) 1129.

[34] B. Schaffer, W. Grogger, G. Kothleitner, Ultramicroscopy 102 (2004) 27.